Supplementary Text

A note on the interpretation of drug treatments on ER motion

At first glance, the ability of a wide range of drugs to alter or reduce ER motion is an intriguing but puzzling finding, since the pharmacological treatments selected affect highly diverse components of cellular biology. However, despite their apparent diversity, all of the treatments used target systems within the cell that are known to be major consumers of cellular energy sources. A number of studies have suggested that living cells have local fluctuations in cytoplasmic pressure as a result of many active intracellular forces, some of which have known origins (*40-43*). These fluctuations are dependent on cellular energy sources. These cytoplasmic variations in local pressure seemed a possible source for ER motion. Consequently, drug treatments were selected to target several of the most fundamental, energy-consuming processes in cells, and it is thus not surprising that they had markedly similar and dramatic effects on ER motion. Some notes on the reason for selecting each treatment are given below:

Depletion of cellular ATP was achieved using DOG + NaN_3 as has been previously characterized, and the treatment was independently verified to have been functional by confirming the significant reduction of motion in the actin cytoskeleton (data not shown). This treatment has been previously demonstrated to reduce cytoplasmic fluctuations to a level consistent with purely thermal contributions after 1 h of treatment (*44*).

Block of access to cellular energy sources was accomplished by treatment with AlF, which locks trimeric G-proteins in a false GTP-bound state. This condition has been shown to broadly block cellular access to energy stored in the form of GTP and a significant proportion of energy stored in the form of ATP.

Inhibition of a major subset of actomyosin-based motor proteins was achieved by treatment with a high concentration of Blebbistatin, a myosin II inhibitor. This drug has previously been demonstrated to halt a significant proportion of actin cytoskeleton dynamics and is known to substantially reduce cytoplasmic fluctuations (*44*).

Microtubule depolymerization was attained using a high dose of nocodazole, as microtubule-based motor proteins are thought to be a substantial contributor to cytoplasmic motion (*45*).

Cellular translation was blocked using two separate treatments, one that leaves the ribosome-RNA complex intact (CHX) and another that causes its dissociation (Puromycin). Both of these reduced ER motion in a similar manner to energy depletion. Translation has been estimated to be the utilizer of up to 20% of cellular energy (reviewed in (*46*)), but to the best of our knowledge it has not been directly tested as a source of cytoplasmic motion.

We therefore conclude that ER motion appears to be broadly linked to cellular energy consumption, but it is not yet clear if this is the direct result of cellular forces causing random motion in the cytoplasm or not.

A note on the size and lifespan of spaces

As reported in the main text, the relocation of the fluorescent protein tag from the membrane (Sec61β) to lumen of the ER (ER3) results in the appearance of smaller

diameter tubules and thus larger measureable gaps between tubules. Thus, a luminal marker, such as ER3, not only gives the appearance of larger distances between tubules, but also allows smaller spaces between the tubules to be measured. We find there is a direct correlation between the size and lifespan of spaces (data not shown), with larger spaces lasting longer than small spaces. It then follows that with a luminal ER marker, more short lived spaces can be measured due to the ability to distinguish between more tightly packed tubules, as seen in Fig. 2D and tables S3 and S4. These results are most consistent with a model of the ER that is a dense array of tubular matrices as opposed to fenestrated sheets. Assuming that tubes and junction on average are moving at similar speeds, the spaces between them would then disappear more quickly if the tubes are closer and more slowly if the tubes are sparse.

Rationale for the selection of FIB-SEM

The optical imaging techniques presented in this paper are able to resolve the structure of ER matrices most readily in the thin periphery of cells, where the cell is in the range of hundreds of nanometers thick. Indeed, when we measure the span between plasma membranes in a FIB-SEM cross-section, we find the distance to average 900 ± 300 nm (fig. S5). While it is possible that ER matrices are also located in the thicker, denser regions of the cell closer to the nucleus, it seemed prudent to choose an electron microscopy approach that would maximize our chances of (i) finding structures in thin regions of cells that are close to the coverslip and (ii) being able to resolve structures that may exist within this small range above the coverslip.

Most successful three dimensional EM reconstructions of the ER have been performed using serial-section or serial block-face scanning approaches (*24, 25*). While these approaches are optimal for tissue sections, they can be technically challenging to perform on coverslip-grown cells where the region abutting the coverslip is of critical importance. By contrast, traditional approaches for this region, such as cellular unroofing followed by platinum replica EM, do not leave the ER attached to the sample, while whole-mount approaches fail to provide sufficient information in the *z* dimension. FIB-SEM has been successfully used to look in a variety of tissues and cell types, and provides an advantage in that milling using a fine atomic beam can result in *z* steps as fine as the resolution in *x* and *y*. In our experiments, this resulted in isotropic 8 nm voxels, which substantially simplified the registration process and avoided many of the issues that can complicate serial section approaches such as tears, folds, and damaged slices. In practice, this also greatly improved our ability to appreciate small height changes in thin structures like many ER matrices. For example, the raw FIB-SEM data for the region in the box shown in Fig. 5A is shown compared to simulated data that would be acquired using a serial sectioning technique with 32 nm slices (fig. S6).

Notes on protein heterogeneity in ER matrices

At first glance, the heterogeneity of ER shaping protein localization within matrices is quite curious. The localization of RTN isoforms and CLIMP63 (Figs. 6 and S2) are quite striking, with examples of both inclusion and exclusion for every protein tested. While antibody staining could potentially lead to low labeling density within sufficiently dense structures, this would not be predicted to affect genetic tags and overexpression experiments. Conversely, overexpression could drive internalization of

proteins into structures where they would not otherwise be located, but this would not be seen in endogenous labeling. Thus, we conclude that at least for some ER shaping proteins (i.e. RTN4A/B + CLIMP63), there may be distinct subsets of ER matrix where the proteins can be enriched, present, or excluded. Whether this correlates with the highly variable matrix structures observed in FIB-SEM (Fig. 5) remains to be seen.

There are many variables that could contribute to this heterogeneity. It is conceivable that some RTN isoforms could be excluded from dense matrices of tubules for a variety of reasons such as: (i) enrichment of other protein within tubular matrices displacing RTNs; (ii) tubules packed at high density could have a net curvature that is incompatible with the curvature stabilizing properties of some RTN isoforms; or (ii) the highly dynamic nature of tubular matrices may be incompatible with the stability of oligomeric RTN complexes, as is evidenced by their low diffusion coefficients in a variety of studies (*20*). The role of CLIMP63 in these structures is less clear. Certainly, CLIMP63 has been implicated in stabilizing the luminal spacing in intact sheets (at approximately 50 nm, (*2*)), but there is no *a priori* reason why it may not also be able to stabilize the luminal diameter of tubules or tubular matrices in a similar way. Furthermore, serial section EM studies in primary neurons have implicated CLIMP63 in causing regions of ER complexity, which are "not sheet-like" in nature (*47*), suggesting this protein may also be able to play an important role in producing and maintaining tubular structures.

Atlastin Isoform Usage

Exogenous expression experiments using ATLs were performed using ATL1 due to the availability of reagents and extensive literature on the protein (*3*). The cellular localization of HaloTag-ATL1 construct was verified by cotransfecting HeLa cells with mEmerald-Sec61β, HaloTag-ATL1 and Myc-ATL1 (fig. S7). Immunocytochemistry was carried out as detailed above. Both ATL1 constructs localize to the ER, demonstrating high colocalization with one another in the periphery. Any minor discrepancies in localization between the Myc- and HaloTag-ATL1 in the perinuclear region are likely due to antibody penetration during the staining protocol.

For endogenous localization experiments, we utilized an antibody to ATL3 since this is the predominant ATL isoform in most non-neuronal cell lines. ATL3 is believed to function in a homologous manner to ATL1 (*48*). Furthermore, in HeLa cells overexpressing mEmerald-Sec61β, HA-ATL3 and Myc-ATL1, both ATL isoforms localize to very similar regions of peripheral ER (fig. S8).

References

1. T. Shemesh, R. W. Klemm, F. B. Romano, S. Wang, J. Vaughan, X. Zhuang, H. Tukachinsky, M. M. Kozlov, T. A. Rapoport, A model for the generation and interconversion of ER morphologies. *Proc. Natl. Acad. Sci. U.S.A.* 111, E5243–E5251 (2014). Medline doi:10.1073/pnas.1419997111

2. Y. Shibata, T. Shemesh, W. A. Prinz, A. F. Palazzo, M. M. Kozlov, T. A. Rapoport, Mechanisms determining the morphology of the peripheral ER. *Cell* 143, 774–788 (2010). Medline doi:10.1016/j.cell.2010.11.007

3. U. Goyal, C. Blackstone, Untangling the web: Mechanisms underlying ER network formation. *Biochim. Biophys. Acta* 1833, 2492–2498 (2013). Medline doi:10.1016/j.bbamcr.2013.04.009

4. C. Blackstone, Cellular pathways of hereditary spastic paraplegia. *Annu. Rev. Neurosci.* 35, 25–47 (2012). Medline doi:10.1146/annurev-neuro-062111-150400

5. C. Lee, L. B. Chen, Dynamic behavior of endoplasmic reticulum in living cells. *Cell* 54, 37–46 (1988). Medline doi:10.1016/0092-8674(88)90177-8

6. A. R. English, G. K. Voeltz, Rab10 GTPase regulates ER dynamics and morphology. *Nat. Cell Biol.* 15, 169–178 (2013). Medline doi:10.1038/ncb2647

7. D. Li, L. Shao, B. C. Chen, X. Zhang, M. Zhang, B. Moses, D. E. Milkie, J. R. Beach, J. A. Hammer 3rd, M. Pasham, T. Kirchhausen, M. A. Baird, M. W. Davidson, P. Xu, E. Betzig, Extended-resolution structured illumination imaging of endocytic and cytoskeletal dynamics. *Science* 349, aab3500 (2015). Medline doi:10.1126/science.aab3500

8. I. Arganda-Carreras, R. Fernández-González, A. Muñoz-Barrutia, C. Ortiz-De-Solorzano, 3D reconstruction of histological sections: Application to mammary gland tissue. *Microsc. Res. Tech.* 73, 1019–1029 (2010). Medline doi:10.1002/jemt.20829

9. S. Chen, T. Desai, J. A. McNew, P. Gerard, P. J. Novick, S. Ferro-Novick, Lunapark stabilizes nascent three-way junctions in the endoplasmic reticulum. *Proc. Natl. Acad. Sci. U.S.A.* 112, 418–423 (2015). Medline doi:10.1073/pnas.1423026112

10. R. Metzler, J. Klafter, The random walk's guide to anomalous diffusion: A fractional dynamics approach. *Phys. Rep.* 339, 1–77 (2000). doi:10.1016/S0370-1573(00)00070-3

11. M. Guo, A. J. Ehrlicher, M. H. Jensen, M. Renz, J. R. Moore, R. D. Goldman, J. Lippincott-Schwartz, F. C. Mackintosh, D. A. Weitz, Probing the stochastic, motor-driven properties of the cytoplasm using force spectrum microscopy. *Cell* 158, 822–832 (2014). Medline doi:10.1016/j.cell.2014.06.051

12. C. Kural, A. S. Serpinskaya, Y. H. Chou, R. D. Goldman, V. I. Gelfand, P. R. Selvin, Tracking melanosomes inside a cell to study molecular motors and their interaction. *Proc. Natl. Acad. Sci. U.S.A.* 104, 5378–5382 (2007). Medline doi:10.1073/pnas.0700145104

13. K. Jaqaman, D. Loerke, M. Mettlen, H. Kuwata, S. Grinstein, S. L. Schmid, G. Danuser, Robust single-particle tracking in live-cell time-lapse sequences. *Nat. Methods* 5, 695–702 (2008). Medline doi:10.1038/nmeth.1237

14. W. R. Legant, L. Shao, J. B. Grimm, T. A. Brown, D. E. Milkie, B. B. Avants, L. D. Lavis, E. Betzig, High-density three-dimensional localization microscopy across large volumes. *Nat. Methods* 13, 359–365 (2016). Medline doi:10.1038/nmeth.3797

15. B.-C. Chen, W. R. Legant, K. Wang, L. Shao, D. E. Milkie, M. W. Davidson, C. Janetopoulos, X. S. Wu, J. A. Hammer 3rd, Z. Liu, B. P. English, Y. Mimori-Kiyosue, D. P. Romero, A. T. Ritter, J. Lippincott-Schwartz, L. Fritz-Laylin, R. D. Mullins, D. M. Mitchell, J. N. Bembenek, A. C. Reymann, R. Böhme, S. W. Grill, J. T. Wang, G. Seydoux, U. S. Tulu, D. P. Kiehart, E. Betzig, Lattice light-sheet microscopy: Imaging molecules to embryos at high spatiotemporal resolution. *Science* 346, 1257998 (2014). Medline doi:10.1126/science.1257998

16. M. Terasaki, T. Shemesh, N. Kasthuri, R. W. Klemm, R. Schalek, K. J. Hayworth, A. R. Hand, M. Yankova, G. Huber, J. W. Lichtman, T. A. Rapoport, M. M. Kozlov, Stacked endoplasmic reticulum sheets are connected by helicoidal membrane motifs. *Cell* 154, 285–296 (2013). Medline doi:10.1016/j.cell.2013.06.031

17. J. Hu, Y. Shibata, P. P. Zhu, C. Voss, N. Rismanchi, W. A. Prinz, T. A. Rapoport, C. Blackstone, A class of dynamin-like GTPases involved in the generation of the tubular ER network. *Cell* 138, 549–561 (2009). Medline doi:10.1016/j.cell.2009.05.025

18. G. Orso, D. Pendin, S. Liu, J. Tosetto, T. J. Moss, J. E. Faust, M. Micaroni, A. Egorova, A. Martinuzzi, J. A. McNew, A. Daga, Homotypic fusion of ER membranes requires the dynamin-like GTPase atlastin. *Nature* 460, 978–983 (2009). Medline doi:10.1038/nature08280

19. G. K. Voeltz, W. A. Prinz, Y. Shibata, J. M. Rist, T. A. Rapoport, A class of membrane proteins shaping the tubular endoplasmic reticulum. *Cell* 124, 573–586 (2006). Medline doi:10.1016/j.cell.2005.11.047

20. Y. Shibata, C. Voss, J. M. Rist, J. Hu, T. A. Rapoport, W. A. Prinz, G. K. Voeltz, The reticulon and DP1/Yop1p proteins form immobile oligomers in the tubular endoplasmic reticulum. *J. Biol. Chem.* 283, 18892–18904 (2008). Medline doi:10.1074/jbc.M800986200

21. G. Stefano, L. Renna, F. Brandizzi, The endoplasmic reticulum exerts control over organelle streaming during cell expansion. *J. Cell Sci.* 127, 947–953 (2014). Medline doi:10.1242/jcs.139907

22. M. W. Hetzer, The nuclear envelope. *Cold Spring Harb. Perspect. Biol.* 2, a000539 (2010). Medline doi:10.1101/cshperspect.a000539

23. R. Fernández-Busnadiego, Y. Saheki, P. De Camilli, Three-dimensional architecture of extended synaptotagmin-mediated endoplasmic reticulum-plasma membrane

contact sites. *Proc. Natl. Acad. Sci. U.S.A.* 112, E2004–E2013 (2015). Medline doi:10.1073/pnas.1503191112

24. M. Puhka, M. Joensuu, H. Vihinen, I. Belevich, E. Jokitalo, Progressive sheet-to-tubule transformation is a general mechanism for endoplasmic reticulum partitioning in dividing mammalian cells. *Mol. Biol. Cell* 23, 2424–2432 (2012). Medline doi:10.1091/mbc.E10-12-0950

25. M. Puhka, H. Vihinen, M. Joensuu, E. Jokitalo, Endoplasmic reticulum remains continuous and undergoes sheet-to-tubule transformation during cell division in mammalian cells. *J. Cell Biol.* 179, 895–909 (2007). Medline doi:10.1083/jcb.200705112

26. P.-P. Zhu, C. Soderblom, J.-H. Tao-Cheng, J. Stadler, C. Blackstone, SPG3A protein atlastin-1 is enriched in growth cones and promotes axon elongation during neuronal development. *Hum. Mol. Genet.* 15, 1343–1353 (2006). Medline doi:10.1093/hmg/ddl054

27. J. Riedl, A. H. Crevenna, K. Kessenbrock, J. H. Yu, D. Neukirchen, M. Bista, F. Bradke, D. Jenne, T. A. Holak, Z. Werb, M. Sixt, R. Wedlich-Soldner, Lifeact: A versatile marker to visualize F-actin. *Nat. Methods* 5, 605–607 (2008). Medline doi:10.1038/nmeth.1220

28. W. He, Y. Lu, I. Qahwash, X. Y. Hu, A. Chang, R. Yan, Reticulon family members modulate BACE1 activity and amyloid-β peptide generation. *Nat. Med.* 10, 959–965 (2004). Medline doi:10.1038/nm1088

29. C. W. Lai, D. E. Aronson, E. L. Snapp, BiP availability distinguishes states of homeostasis and stress in the endoplasmic reticulum of living cells. *Mol. Biol. Cell* 21, 1909–1921 (2010). Medline doi:10.1091/mbc.E09-12-1066

30. E. L. Snapp, A. Sharma, J. Lippincott-Schwartz, R. S. Hegde, Monitoring chaperone engagement of substrates in the endoplasmic reticulum of live cells. *Proc. Natl. Acad. Sci. U.S.A.* 103, 6536–6541 (2006). Medline doi:10.1073/pnas.0510657103

31. J. B. Grimm, B. P. English, J. Chen, J. P. Slaughter, Z. Zhang, A. Revyakin, R. Patel, J. J. Macklin, D. Normanno, R. H. Singer, T. Lionnet, L. D. Lavis, A general method to improve fluorophores for live-cell and single-molecule microscopy. *Nat. Methods* 12, 244–250 (2015). Medline doi:10.1038/nmeth.3256

32. N. B. Cole, Compendium of drugs commonly used in cell biology research. *Curr. Protoc. Cell Biol.* 00:1B:1.B.1–1.B.26 (1998).

33. J. G. Donaldson, R. A. Kahn, J. Lippincott-Schwartz, R. D. Klausner, Binding of ARF and beta-COP to Golgi membranes: Possible regulation by a trimeric G protein. *Science* 254, 1197–1199 (1991). Medline doi:10.1126/science.1957170

34. J. A. Steyer, W. Almers, A real-time view of life within 100 nm of the plasma membrane. *Nat. Rev. Mol. Cell Biol.* 2, 268–275 (2001). Medline doi:10.1038/35067069

35. T. J. Deerinck, E. A. Bushong, A. Thor, M. H. Ellisman, NCMIR methods for 3D EM: A new protocol for preparation of biological specimens for serial block face scanning electron microscopy (National Center for Microscopy and Imaging Research, 2010); www.ncmir.ucsd.edu/sbem-protocol.

36. P. Kner, B. B. Chhun, E. R. Griffis, L. Winoto, M. G. L. Gustafsson, Super-resolution video microscopy of live cells by structured illumination. *Nat. Methods* 6, 339–342 (2009). Medline doi:10.1038/nmeth.1324

37. C. Sommer, C. Straehle, U. Kothe, F. A. Hamprecht, Ilastik: Interactive learning and segmentation toolkit. In *2011 8th IEEE International Symposium on Biomedical Imaging (ISBI 2011)*, pp. 230–233 (2011). doi:10.1109/ISBI.2011.5872394

38. D. Loerke, M. Mettlen, D. Yarar, K. Jaqaman, H. Jaqaman, G. Danuser, S. L. Schmid, Cargo and dynamin regulate clathrin-coated pit maturation. *PLOS Biol.* 7, e1000057 (2009). Medline doi:10.1371/journal.pbio.1000057

39. A. V. Weigel, M. M. Tamkun, D. Krapf, Quantifying the dynamic interactions between a clathrin-coated pit and cargo molecules. *Proc. Natl. Acad. Sci. U.S.A.* 110, E4591–E4600 (2013). Medline doi:10.1073/pnas.1315202110

40. A. D. Doyle, K. M. Yamada, Cell biology: Sensing tension. *Nature* 466, 192–193 (2010). Medline doi:10.1038/466192a

41. Y. F. Dufrêne, E. Evans, A. Engel, J. Helenius, H. E. Gaub, D. J. Müller, Five challenges to bringing single-molecule force spectroscopy into living cells. *Nat. Methods* 8, 123–127 (2011). Medline doi:10.1038/nmeth0211-123

42. G. G. Gundersen, H. J. Worman, Nuclear positioning. *Cell* 152, 1376–1389 (2013). Medline doi:10.1016/j.cell.2013.02.031

43. C.-P. Heisenberg, Y. Bellaïche, Forces in tissue morphogenesis and patterning. *Cell* 153, 948–962 (2013). Medline doi:10.1016/j.cell.2013.05.008

44. M. Guo, A. J. Ehrlicher, M. H. Jensen, M. Renz, J. R. Moore, R. D. Goldman, J. Lippincott-Schwartz, F. C. Mackintosh, D. A. Weitz, Probing the stochastic, motor-driven properties of the cytoplasm using force spectrum microscopy. *Cell* 158, 822–832 (2014). Medline doi:10.1016/j.cell.2014.06.051

45. R. D. Vale, The molecular motor toolbox for intracellular transport. *Cell* 112, 467–480 (2003). Medline doi:10.1016/S0092-8674(03)00111-9

46. D. F. Rolfe, G. C. Brown, Cellular energy utilization and molecular origin of standard metabolic rate in mammals. *Physiol. Rev.* 77, 731–758 (1997). Medline

47. T. Cui-Wang, C. Hanus, T. Cui, T. Helton, J. Bourne, D. Watson, K. M. Harris, M. D. Ehlers, Local zones of endoplasmic reticulum complexity confine cargo in neuronal dendrites. *Cell* 148, 309–321 (2012). Medline doi:10.1016/j.cell.2011.11.056

48. N. Rismanchi, C. Soderblom, J. Stadler, P.-P. Zhu, C. Blackstone, Atlastin GTPases are required for Golgi apparatus and ER morphogenesis. *Hum. Mol. Genet.* 17, 1591–1604 (2008). Medline doi:10.1093/hmg/ddn046

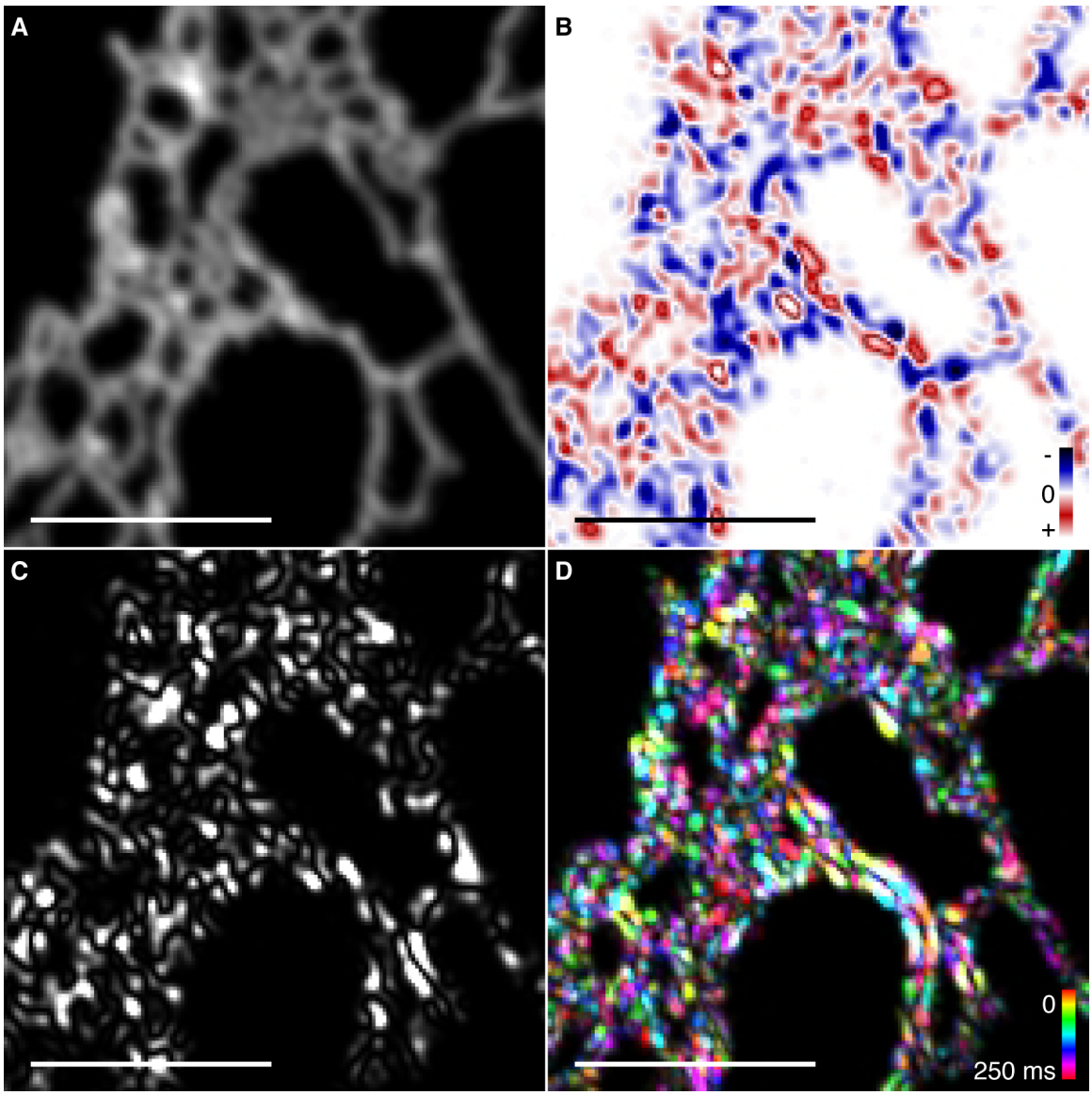

Fig. S1.

Method for temporal derivative. **(A)** An image acquired and reconstructed by GI-SIM, smoothed using a Gaussian filter with σ = 45 nm and bleach corrected using the histogram-matching algorithm in ImageJ. **(B)** Each frame is subtracted from the subsequent frame. **(C)** The resulting image is squared. **(D)** The derivative is temporally color-coded over the length of the time-lapse image. Scale bars, 2 μm.

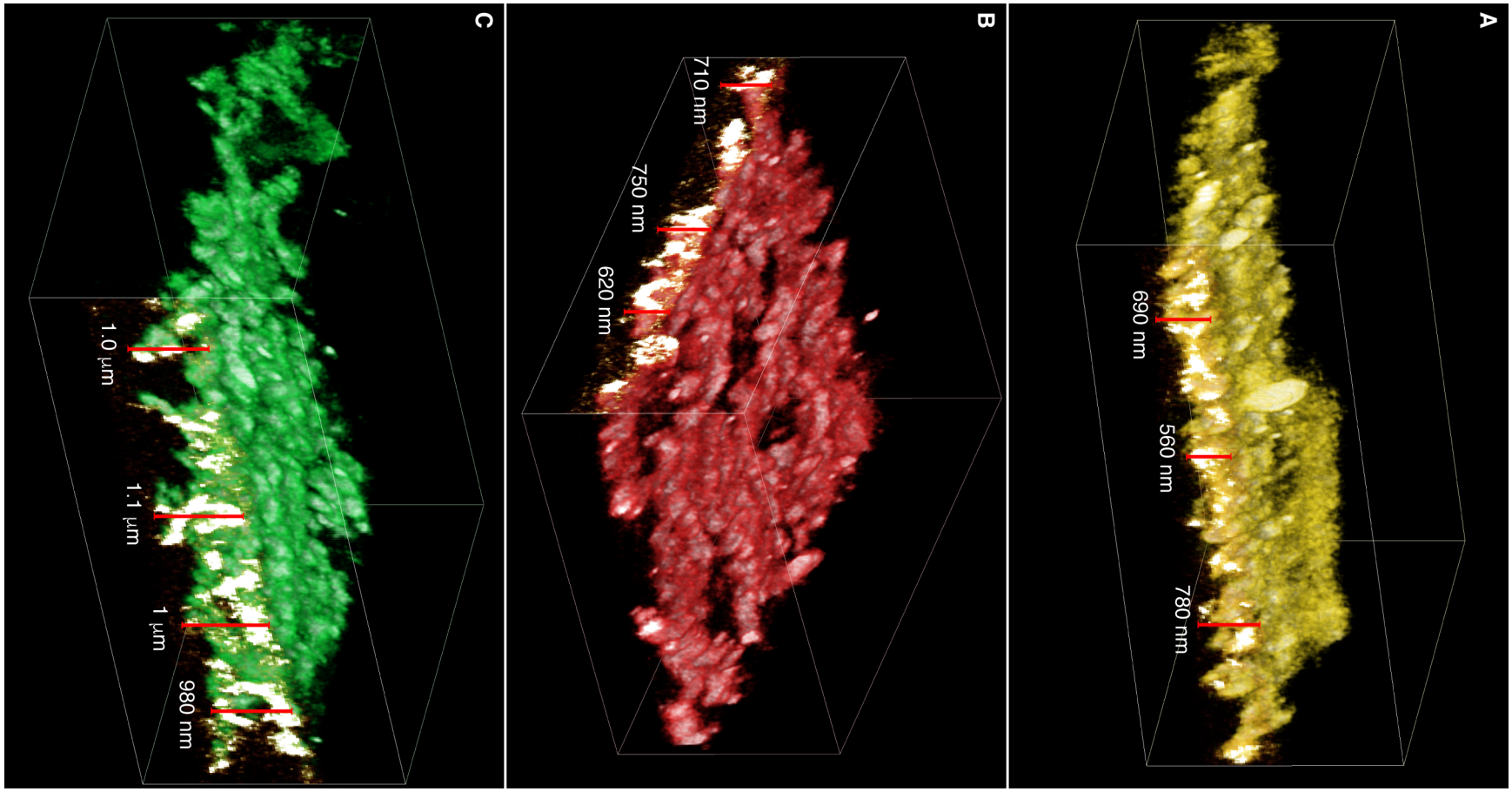

Fig. S2.

The ER is three-dimensional in nature even in thin regions of the cell. (A-C) Cross-sections through the LLS-PAINT data shown in Fig. 3B. Despite some ER matrices being relatively flat, when imaged with sufficiently high resolution in the *z* dimension substantial topology can be observed.

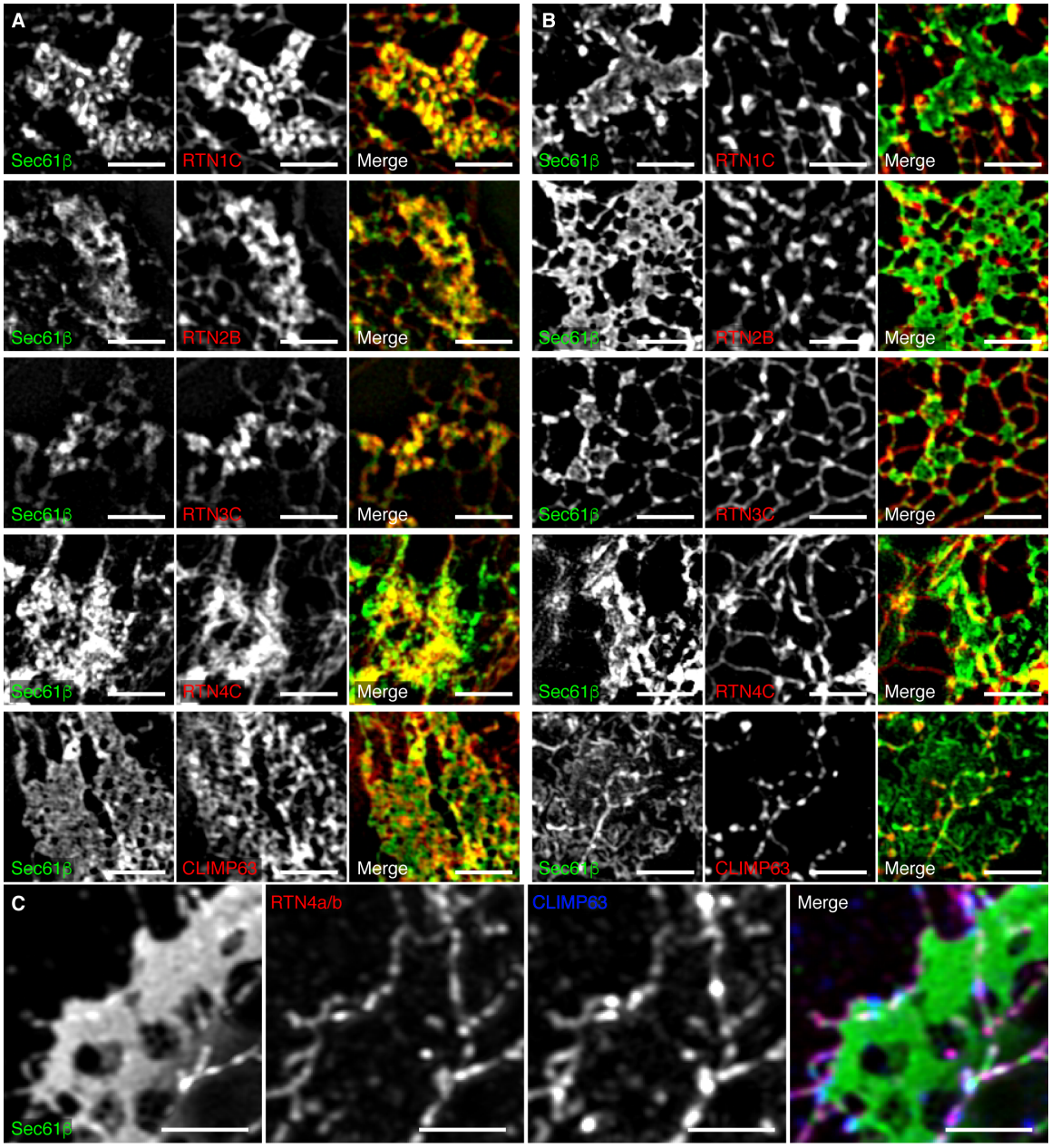

Fig. S3.

Traditional ER-shaping proteins show heterogeneity in matrix localization. Fixed COS-7 cells expressing mEmerald-Sec61β and an ER-shaping protein imaged by 3D-SIM. Examples of inclusion **(A)** within dense tubular matrices and exclusion **(B)** for each ER shaping protein. **(C)** A U-2 OS cell expressing mEmerald-Sec61β stained for endogenous RTN4A/B and CLIMP63, illustrating exclusion from a dense tubular matrix. Scale bars, 2 μm.

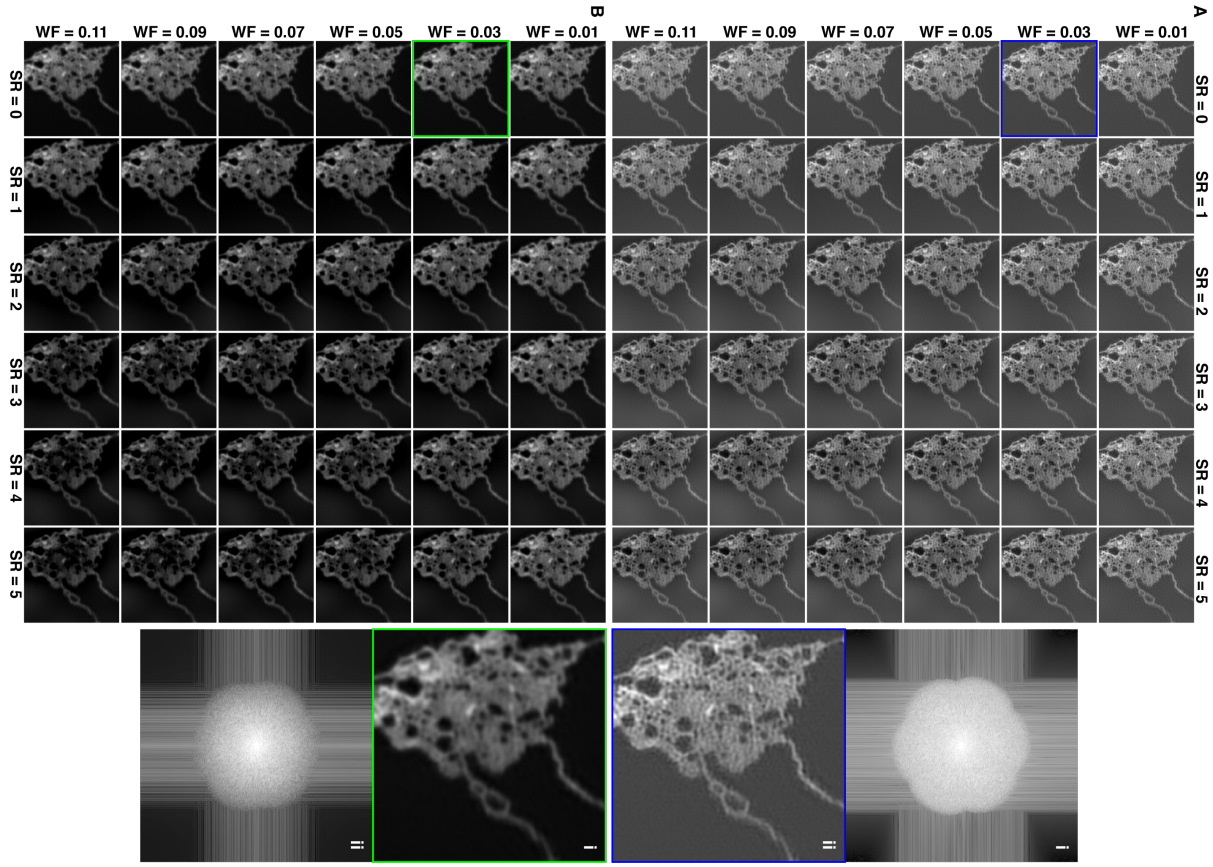

Fig. S4.

Optimization of SIM reconstructions. A comprehensive analysis of critical SIM reconstruction steps to minimize any reconstruction-based artifacts. **(A)** Wiener filter vs a notch filter localized at the peaks at Abbe's limit, with the indicated suppression radius (SR), no Gaussian blurring. **(B)** Wiener filter vs a notch filter (as above), with σ = 45nm radius Gaussian blur. Colored boxes **(i)** denote settings that were used for this particular image (WF = 0.03, SR = 0) with (green box) and without (blue box) Gaussian blurring and their corresponding optical transfer function **(ii)**

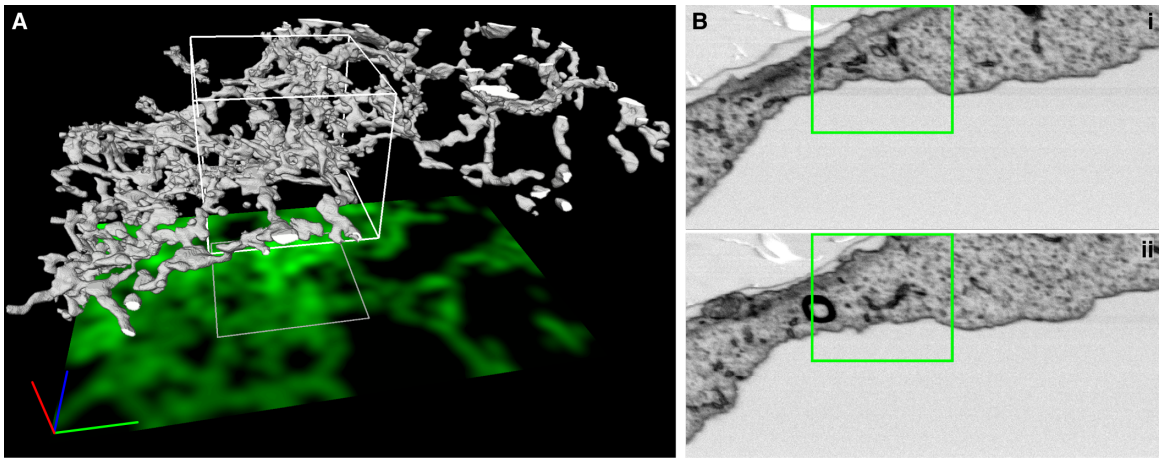

Fig. S5.

Measuring the thin periphery of cells. (A) FIB-SEM reconstruction of an ER matrix, reproduced from Fig. 5B. **(B)** FIB-SEM slices of the area in (A) in the *x*-*z* plane (red-green axis) with boxed region shown for orientation. Slices **(i)** and **(ii)** are spaced by 800 nm in *y* (blue axis). The distance between the plasma membranes within the boxed region is 900 ± 300 nm (n = 21 measurements).

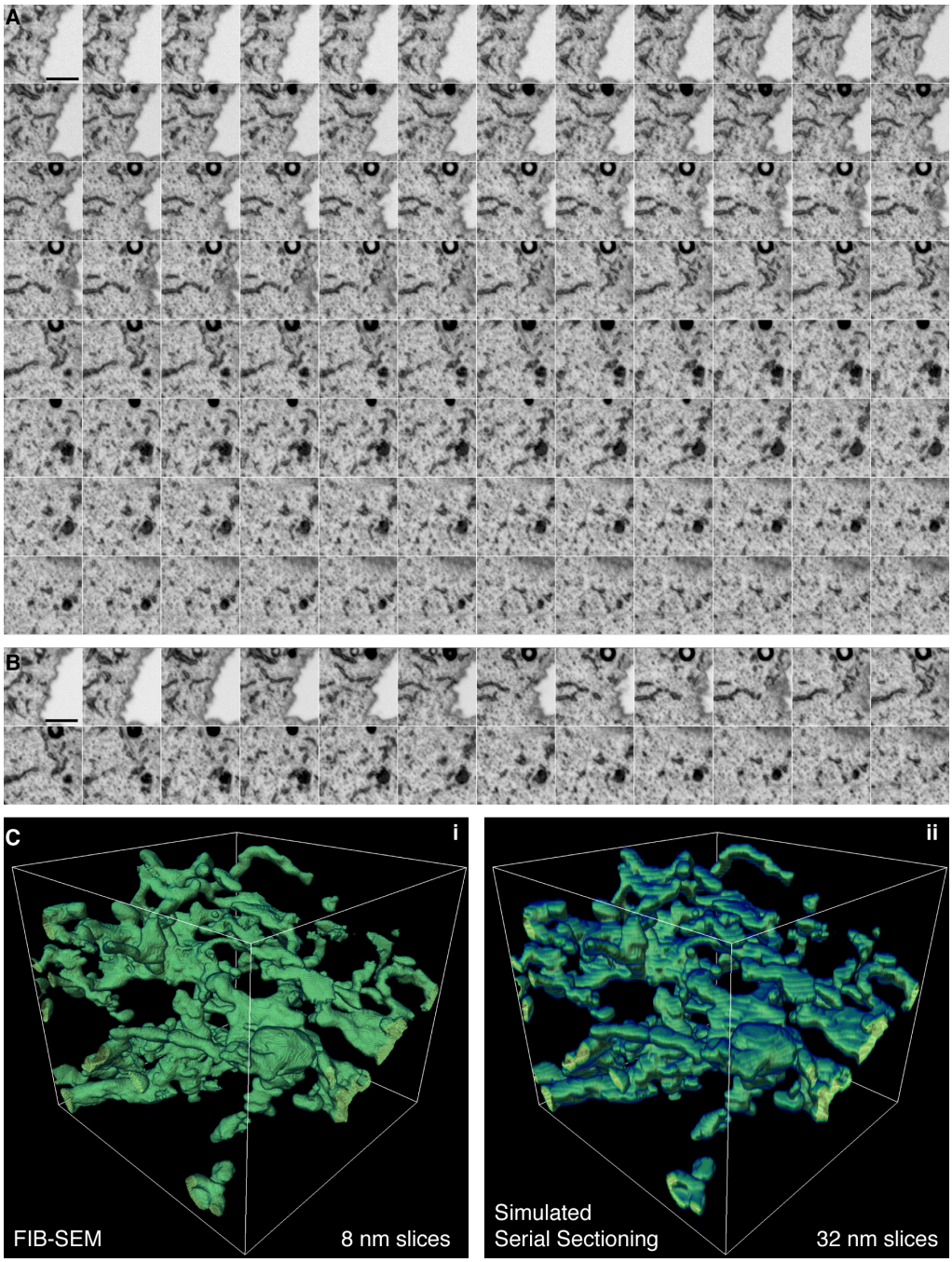

Fig. S6

FIB-SEM provides more information about small changes in z-height than traditional serial section techniques. The raw data collected in the volume indicated by the box in Figure 5B (2.4 x 2.4 μm). **(A)** FIB-SEM using 8 nm steps collects 96 individual slices through this region (786 nm). Scale bar, 1 μm. **(B)** Simulated data collected using a serial section technique with 32 nm thickness per slice (sum of 4 serial FIB-SEM slices) through the same region. Scale bar, 1 μm. **(C)** 3D reconstruction of slices in **(i)** (A) and **(ii)** (B). The loss of detail can be seen in the theoretical serial section technique.

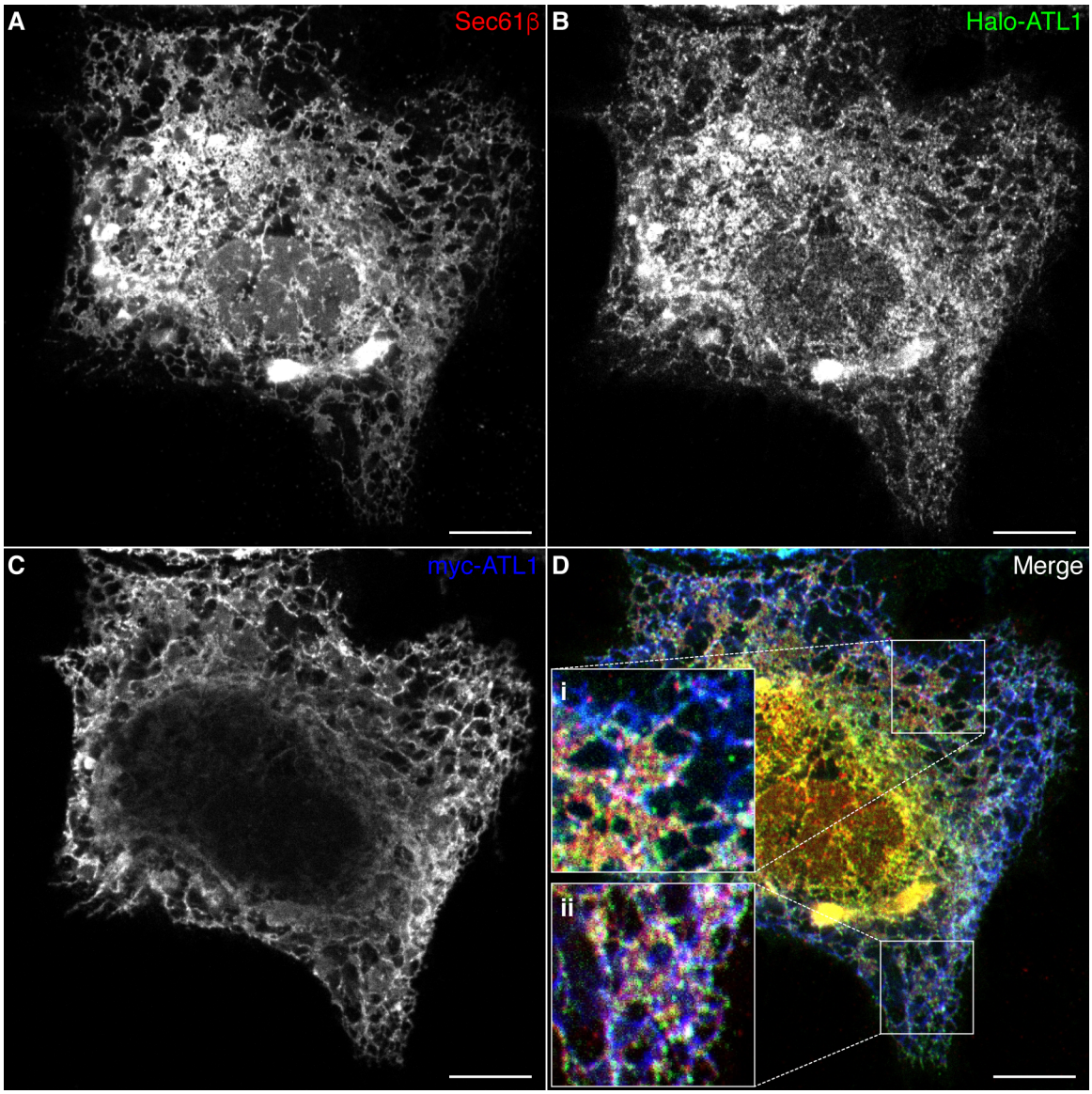

Fig. S7

Introduction of a HaloTag does not perturb ATL1 localization to tubular ER structures. **(A-C)** Fixed HeLa cell expressing mEmerald-Sec61β **(A)**, HaloTag-ATL1 **(B)**, and Myc-ATL1 **(C)** were imaged by scanning point confocal microscopy. **(D)** HaloTag-ATL1 and Myc-ATL1 colocalize at similar regions of ER. The two insets, **(i)** and **(ii)**, in the merged image demonstrate localization of both Myc-ATL1 and HaloTag-ATL1 within structures that appear as sheets. Scale bars, 10 μm.

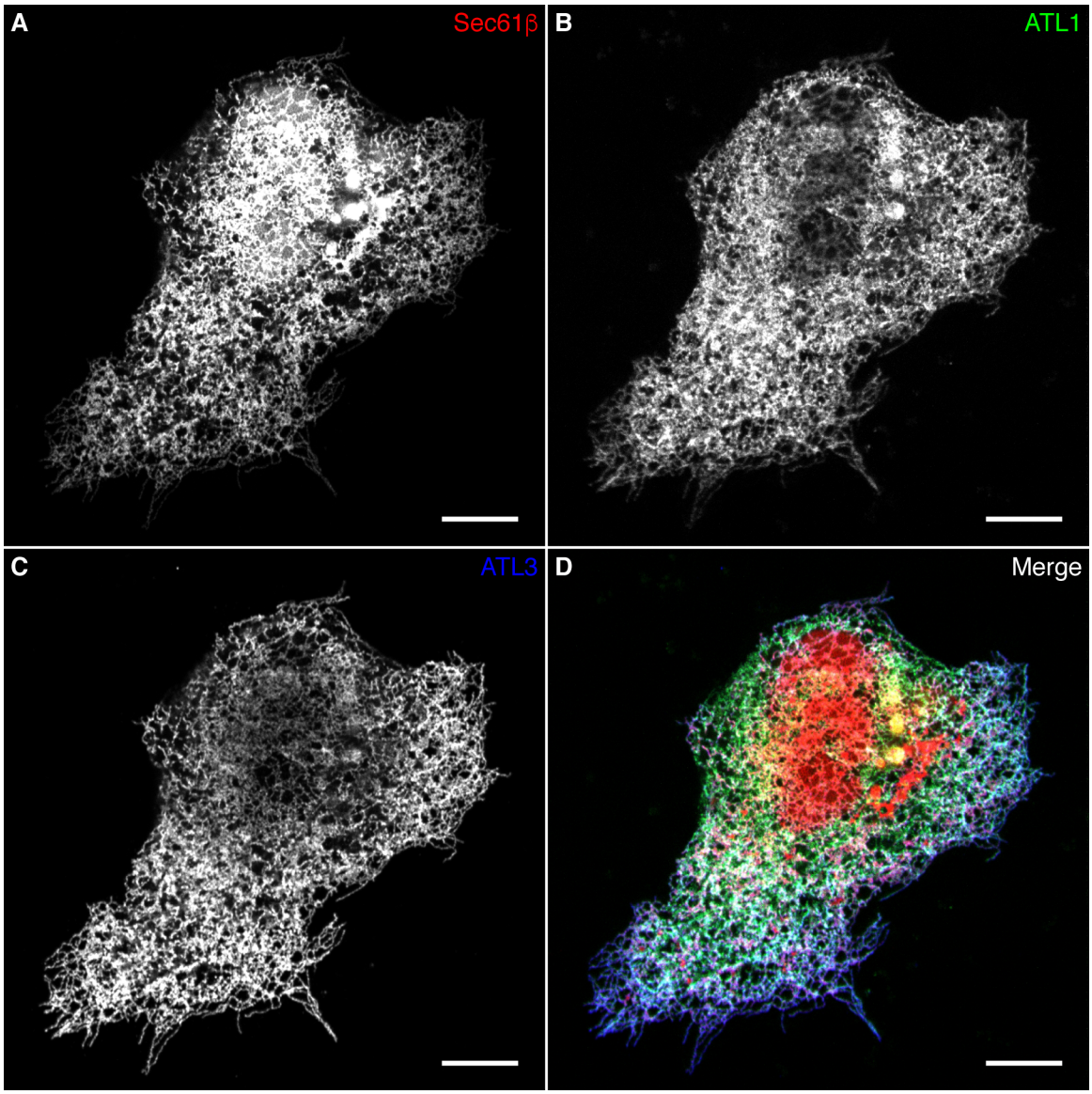

Fig. S8

ATL1 and ATL3 co-localization. Fixed HeLa cell co-expressing mEmerald-Sec61β. (A), Myc-ATL1 **(B)**, and HA-ATL3 **(C)** was imaged using scanning point confocal microscopy. The merged image **(D)** shows that Myc-ATL1 and HA-ATL3 co-localize within similar regions of the ER. Scale bars, 10 μm.

Table S1.

Summary of measurements reported in Fig. 1. The mean peak-to-peak amplitude (Figs. 1C, 1E) and frequency of oscillations (Fig. 1D, 1E) is stated for each treatment, as well as the measured MSD alpha exponents (Fig. 1G) of three-way junctions.

	Condition	*N* (tubules)	*N* (cells)	Amplitude ± SD (nm)	Frequency ± SD (Hz)
Figure 1C, 1D & 1E	Sec61β	1755	8	70 ± 50	4 ± 1
	ER3	3230	19	70 ± 50	4 ± 1
	U-2 OS - Sec61β	610	9	60 ± 50	4 ± 1
	DOG + NaN_3	1080	9	40 ± 20	8 ± 2
	AlF	1291	8	40 ± 20	9 ± 2
	NZ	413	5	70 ± 30	7 ± 2
	Bleb	698	4	40 ± 20	9 ± 3
	Puro	1105	5	40 ± 20	9 ± 2
	CHX	1017	5	50 ± 20	9 ± 2
	Condition	***N* (junctions)**	***N* (cells)**	**Alpha ± SD**	
Figure 1G	Sec61β	313	8	0.5 ± 0.3	
	ER3	279	19	0.4 ± 0.2	
	U-2 OS - Sec61β	148	9	0.4 ± 0.2	
	DOG + NaN_3	273	9	0.1 ± 0.2	
	AlF	186	8	0.2 ± 0.2	
	NZ	57	5	0.3 ± 0.3	
	Bleb	135	4	0.1 ± 0.2	
	Puro	211	5	0.2 ± 0.2	
	CHX	134	5	0.2 ± 0.2	

Table S2.

Testing the populations in Fig. 1 for statistically significant differences in means. A one-way ANOVA was used to test for significant differences between means of the three groups: Sec61bβ, ER3 and U-2 OS - Sec61β. Tukey's multiple comparison post hoc test was then used to test between specific groups. A two-tailed, two sample *t*-test using a Welch correction for non-equal variance was used to test between control (Sec61bβ) and drug treatment groups. Highlighted cells denote statistical significance at the 0.001 level.

ONE-WAY ANOVA

Group 1	*Group 2*	*Group 3*	*Mean amplitude p-value*	*Mean frequency p-value*	*Mean alpha p-value*
Sec61β	ER3	U-2 OS - Sec61β	0.024	2.7E-4	2.2E-4

TUKEY'S MULTIPLE COMPARISON POST HOC TEST

	Group 1	*Group 2*	*Mean amplitude p-value*	*Mean frequency p-value*	*Mean alpha p-value*
	Sec61β	ER3	0.99	0.0089	0.013
	Sec61β	U-2 OS - Sec61β	0.031	0.38	3.6E-4
	ER3	U-2 OS - Sec61β	0.024	0.0020	0.30

TWO SAMPLE *T*-TEST WITH WELCH CORRECTION FOR NON-EQUAL VARIANCE

	Group 1	*Group 2*	*Mean amplitude p-value*	*Mean frequency p-value*	*Mean alpha p-value*
	Sec61β	DOG + NaN_3	1.9E-82	< 1E-230	1.1E-64
	Sec61β	AlF	2.2E-138	< 1E-230	1.2E-47
	Sec61β	NZ	0.54	3.56E-103	1.1E-6
	Sec61β	Bleb	3.6E-137	4.82E-229	1.4E-42
	Sec61β	Puro	1.9E-100	< 1E-230	6.4E-34
	Sec61β	CHX	5.6E-62	< 1E-230	3.3E-30

Table S3.

Summary of measurements reported in Fig. 2. Lifetime of spaces extracted from SPT of inverted sheets (Fig. 2D, top), distance between dense tubules (Fig. 2D, bottom)

	Condition	*N* (spaces)	*N* (cells)	Lifetime ± SD (ms)
Figure 2D (top)	Sec61β	4292	4	250 ± 250
	ER3	1986	5	190 ± 160
	U-2 OS - Sec61β	2009	4	260 ± 240
	Condition	***N* (spaces)**	***N* (cells)**	**Distance ± SD (nm)**
Figure 2D (bottom)	Sec61β	1273	4	260 ± 350
	ER3	1913	5	310 ± 370
	U-2 OS - Sec61β	650	4	300 ± 490

Table S4.

Testing the populations in Figure 2 for statistically significant differences in means. A one-way ANOVA was used to for significant differences between means of the three groups: Sec61bβ, ER3 and U-2 OS - Sec61β. Tukey's multiple comparison post hoc test was then used to test between specific groups. Highlighted cells denote statistical significance at the 0.001 level.

ONE WAY ANOVA

Group 1	*Group 2*	*Group 3*	*Mean lifetime p-value*	*Mean distance p-value*
Sec61β	ER3	U-2 OS - Sec61β	< 1E-230	0.0056

TUKEY'S MULTIPLE COMPARISON POST HOC TEST

	Group 1	*Group 2*	*Mean lifetime p-value*	*Mean distance p-value*
	Sec61β	ER3	3.3E-16	0.0044
	Sec61β	U-2 OS - Sec61β	0.70	0.12
	ER3	U-2 OS - Sec61β	3.3E-16	0.90

Table S5.

Summary of measurements reported in Fig. 4. The effect of temporal blurring (Fig. 4B) and spatial resolution (Fig 4C) on the diameter of tubules. The effect of temporal blurring on the measurable distance between dense tubules (Fig. 4E) and density of spaces (Fig 4F). The effect of spatial blurring on the measurable distance between dense tubules (Fig. 4H) and density of spaces (Fig. 4I).

Figure 4B (live)	**Condition**	***N* (tubes)**	***N* (cells)**	**Diameter ± SD (nm)**
	25 ms	90	3	200 ± 30
	250 ms	92	5	200 ± 20
	1 s	91	5	220 ± 30
Figure 4C (fixed)	**Condition**	***N* (tubes)**	***N* (cells)**	**Diameter ± SD (nm)**
	GI	59	2	270 ± 30
	3D-SIM	145	3	150 ± 20
	PAINT	152	3	120 ± 40
Figure 4E (live)	**Condition**	***N* (spaces)**	***N* (cells)**	**Distance ± SD (nm)**
	25 ms	74	3	150 ± 50
	250 ms	144	5	310 ± 30
	1 s	145	5	410 ± 50
Figure 4F (live)	**Condition**	***N* ("sheets")**	***N* (cells)**	**Density ± SD (μm^{-2})**
	25 ms	18	3	7 ± 3
	250 ms	18	5	5 ± 3
	1 s	18	5	4 ± 2
Figure 4H (fixed)	**Condition**	***N* (spaces)**	***N* (cells)**	**Distance ± SD (nm)**
	GI	131	2	500 ± 200
	3D-SIM	162	4	220 ± 80
	PAINT	46	3	200 ± 200
Figure 4I (fixed)	**Condition**	***N* ("sheets")**	***N* (cells)**	**Density ± SD (μm^{-2})**
	GI	9	2	0.7 ± 0.2
	3D-SIM	30	4	5 ± 1
	PAINT	24	3	7 ± 3

Table S6.

Testing the populations in Figure 4 for statistically significant differences in means. A one-way ANOVA was used to for significant differences between means of the three groups in live (25 ms, 250 ms, 1 s) and fixed (GI, 3D-SIM, PAINT) cells. Tukey's multiple comparison post hoc test was then used to test between specific groups. Highlighted cells denote statistical significance at the 0.001 level.

ONE WAY ANOVA

Group 1	*Group 2*	*Group 3*	*Mean tube diameter p-value*	*Mean distance across spaces p-value*	*Mean density of spaces p-value*
25 ms	250 ms	1 s	2.5E-5	2.1E-6	3.2E-4
GI	3D-SIM	PAINT	< 1E-230	< 1E-230	6.3E-10

TUKEY'S MULTIPLE COMPARISON TEST

	Group 1	*Group 2*	*Mean tube diameter p-value*	*Mean distance across spaces p-value*	*Mean density of spaces p-value*
Live	25 ms	250 ms	0.12	0.0052	0.053
Live	25 ms	1 s	1.4E-5	1.0E-6	1.97E-4
Live	250 ms	1 s	0.019	0.035	0.13
Fixed	GI	3D-SIM	< 1E-230	< 1E-230	2.16E-7
Fixed	GI	PAINT	< 1E-230	< 1E-230	< 1E-230
Fixed	3D-SIM	PAINT	< 1E-230	0.44	0.024

Movie S1.

Tracking of rapid motions of peripheral ER tubules and three-way junctions. A region of a COS-7 cell overexpressing mEmerald-Sec61β imaged at 40 Hz using GI-SIM (leftmost panel). The skeletonized midline of each tubule is depicted in the middle-left panel from which its motion can be calculated (e.g., Fig. 1C). The location of three-way junctions is depicted in the middle-right panel, from which a SPT algorithm was used to extract dynamics (e.g., Fig. 1E). Overlay of all three panels is shown at right. Scale bar, 2 μm.

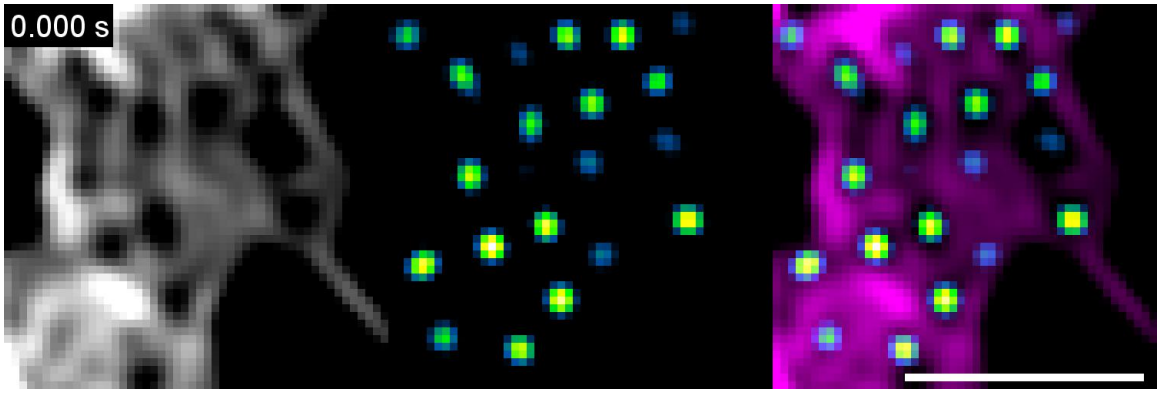

Movie S2.

Peripheral ER "sheets" appear discontinuous. A peripheral sheet from a COS-7 cell overexpressing mEmerald-Sec61β imaged at 40 Hz using GI-SIM (left panel). The middle panel illustrates spaces within the "sheet" derived from inverting the image, subtracting the area outside of the "sheet", and Gaussian smoothing (see Materials and Methods). This permits SPT of spaces. A merge of both the raw data and data processed for illustrating spaces is depicted in the right panel. Scale bar, 2 μm.

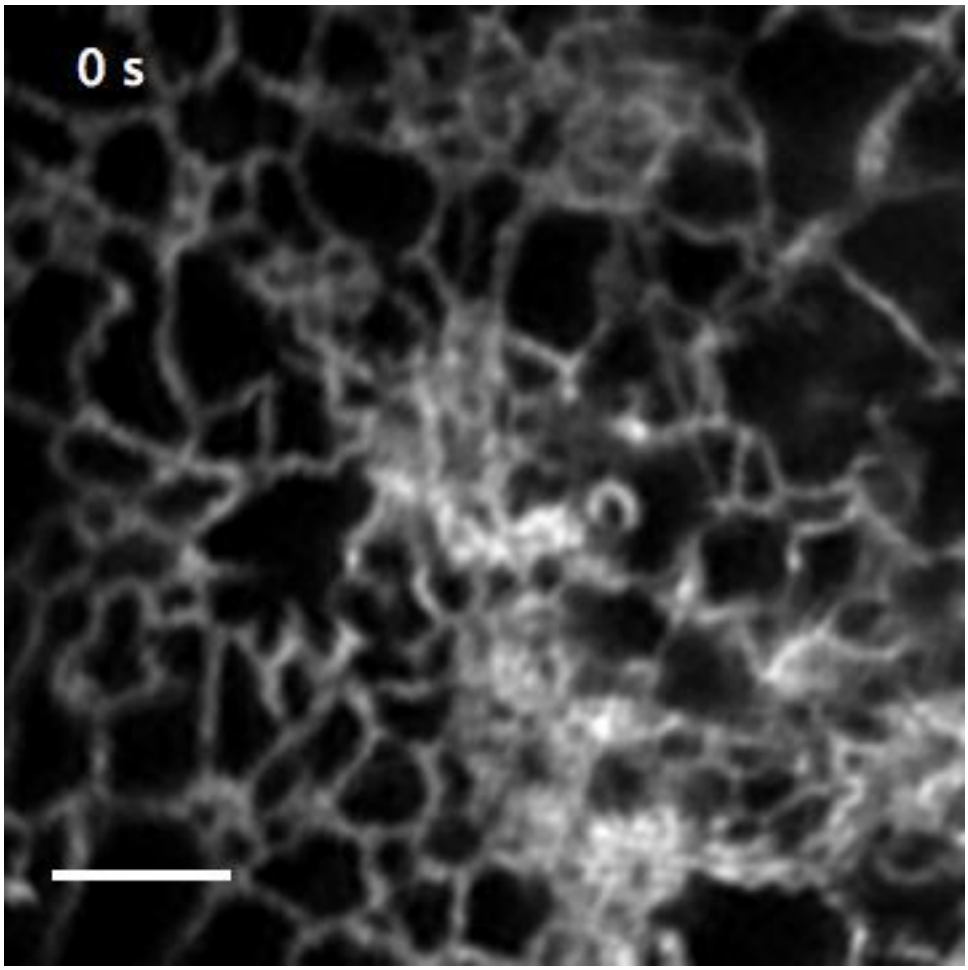

Movie S3.

Rapid assembly and disassembly of peripheral sheet-like structures into tubules. Representative region of a COS-7 cell overexpressing mEmerald-Sec61β imaged using GI-SIM. Each frame was acquired in 25 ms, with a 1 s interval between frames. Rapid moving clusters of tubules and associated three-way junctions appear to rapidly interconvert between 'sheet-like' and clustered three-way junctions. Scale bar, 2 μm.

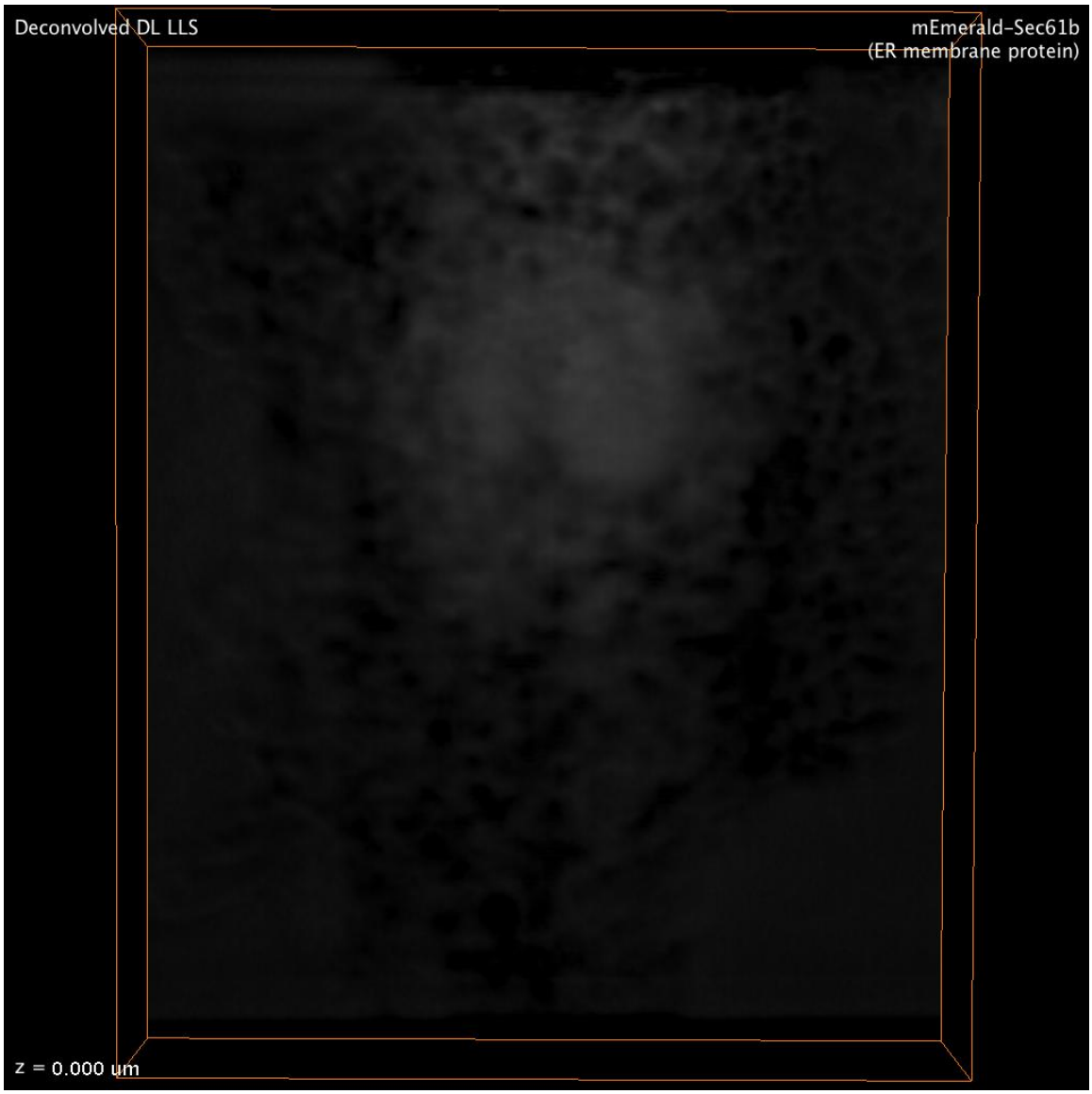

Movie S4.

Internal membranes of a fixed COS-7 cell reconstructed using correlative 3D LLS and LLS-PAINT microscopy. Correlative imaging between mEmerald-Sec61β labeled ER (gray diffraction-limited LLS image) imaged using 3D LSS microscopy, and all lipid membranes labeled with BODIPY-TR and AZEP-Rh (pseudo colored LLS-PAINT image), the latter reconstructed from 549 million localizations.

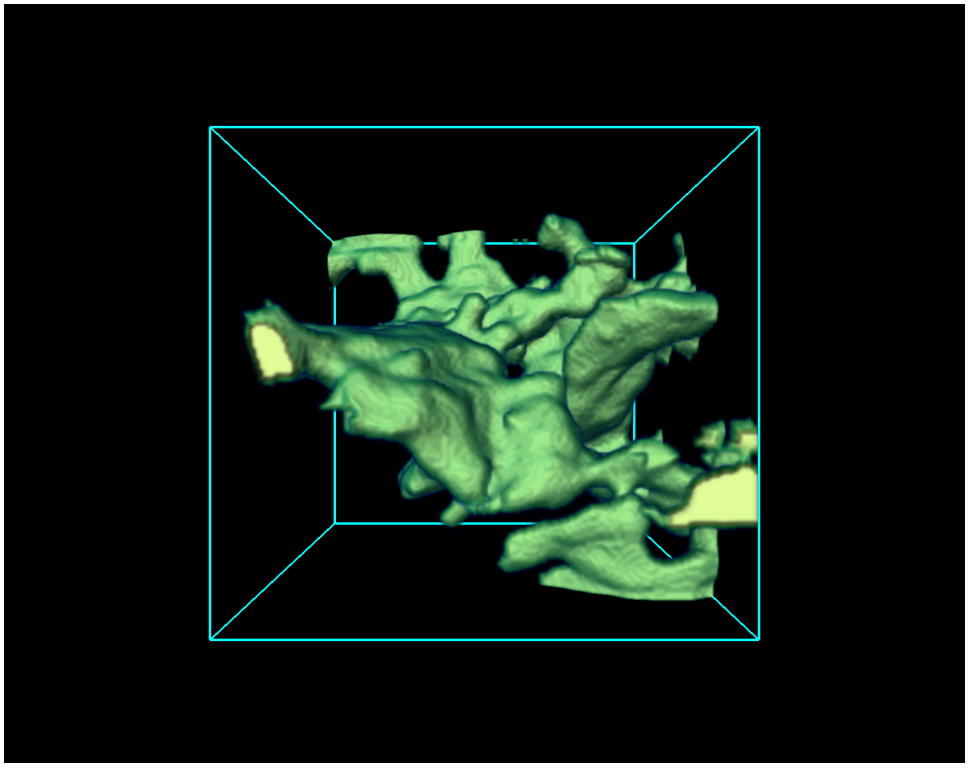

Movie S5.

The structure of a helicoidal sheet by FIB-SEM. The FIB-SEM reconstruction shown in Fig. 5F is reproduced here, to allow more clear demonstration of the helicoidal structure.